RESEARCH

Hydrodynamic coefficients of mussel dropper lines derived from large-scale experiments and structural dynamics

Jannis Landmann[1,2] · Christian Flack[3] · Ursula Kowalsky[3] · Roland Wüchner[3] · Arndt Hildebrandt[1,2] · Nils Goseberg[4,5]

Abstract

The expansion of marine aquaculture production is driven by a high market demand for marine proteins and a stagnation of wild catch of fish. Bivalve farming, i.e., the cultivation of oysters, mussels and scallops, is an important part of the ongoing market dynamics and production expansion. As marine spatial planning is considering various use purposes, available space for near-shore aquaculture is already becoming scarce; this has fueled research and development initiatives to enable production installations further offshore. The highly energetic conditions at more exposed offshore marine sites lead to increased loads on aquaculture systems and their components and it is still not sufficiently understood how the load transfer from oceanic environmental conditions onto shellfish-encrusted surfaces attached to elastic ropes may be appropriately quantified. This study data gathered large-scale data sets in a wave tank facility, which are used to validate a novel, numerical model, building on the dynamics of rope structures which allows for the determination of the hydrodynamic loads transferred to the dropper lines. The forces and hydrodynamic parameters are measured and numerically analyzed. Based on the results, drag and inertia coefficients are determined. A drag coefficient of $C_D = 1.1$ and an inertia coefficient of $C_M = 1.7$ are recommended to model shellfish-encrusted dropper lines exposed to oscillatory flows with KC $= 40$–90. The numerical model for the determination of wave-induced forces on mussel dropper lines is developed and validated using the experimental data. It employs a modified Morison equation, which takes into account the displacement of the mussel dropper line. The influence of varying aquaculture-related parameters is discussed by applying the numerical model. Based on the gathered insights, recommendations can be given from an engineering point of view concerning the optimal placement of mussel aquaculture within the water column.

Keywords Aquaculture engineering · Bivalves · Hydrodynamic coefficients · Drag · Inertia · Mussels · Offshore

✉ Jannis Landmann
  j.landmann@bluec.engineering

  Christian Flack
  c.flack@tu-bs.de

  Ursula Kowalsky
  u.kowalsky@tu-bs.de

  Roland Wüchner
  r.wuechner@tu-bs.de

  Arndt Hildebrandt
  hildebrandt@lufi.uni-hannover.de

  Nils Goseberg
  n.goseberg@tu-bs.de

1 Ludwig-Franzius-Institute for Hydraulic, Estuarine and Coastal Engineering, Leibniz Universität Hannover, Hannover, Germany

2 Blue C GmbH, Brühl, Germany

3 Institute of Structural Analysis, TU Braunschweig, Braunschweig, Germany

4 Leichtweiß-Institute for Hydraulic Engineering and Water Resources, Division Hydromechanics, Coastal and Ocean Engineering, TU Braunschweig, Braunschweig, Germany

5 Coastal Research Center, Joint Research Facility of Leibniz Universität Hannover and Technische Universität Braunschweig, Hannover, Germany

1 Introduction

Bivalve aquaculture, along with the development of innovative cultivation systems, close to shore or in exposed waters, plays a crucial role in establishing fresh sources of protein-rich sustenance essential for supporting the growing global population. By 2100, a population increase by 42% to 9.7 billion people is projected (UN 2023). Of these people,

over a billion are projected to reside in coastal areas (Neumann et al. 2015). As emphasized in the UN's Sustainable Development Goals (SDGs), addressing food security and eliminating hunger for these expanding populations represents a significant challenge for the future. In pursuit of these goals, enhancing nutrition, particularly ensuring a consistent supply of proteins, stands as a top priority. Proteins serve as integral components in next-to-all biological processes (Cozzone 2010). In general, proteins can be obtained from animal- or plant-based sources. In coastal zones, the utilization of marine-based proteins holds significant promise for a sustainable expansion of the resource in view of the described demographic changes as they constitute one of the world's largest sources of animal protein. The development of new aquaculture areas becomes imperative as most on- and nearshore spaces are already occupied, or limited by ecological and sociological factors (Krause et al. 2015). A transition to offshore environments is proposed by politicians, industry, and research officials (Mascorda Cabre et al. 2021; DNV 2021; NOAA 2011). However, it's crucial to acknowledge the increased environmental demands in these high-energy settings when designing aquaculture systems, as these systems will be exposed to considerably higher levels of energy.

Longline systems are regarded as the most viable technology for an expansion of bivalve aquaculture into offshore locations, as document by various studies (Buck 2007; Buck and Langan 2017; Goseberg et al. 2017; Cheney et al. 2010). Longline systems are comprised of a multitude of dropper lines hanging from a horizontally oriented main line, often referred to as a "backbone". Buoyancy is provided to the backbone and connected dropper lines through the use of buoys or other flotation devices. The whole system is conventionally moored, depending on site conditions and the individual dynamics of the system as well as the requirements regarding a dynamic equilibrium in survivability conditions. Figure 1 shows a sketch of a longline backbone with the attached mussel dropper lines, the possible loads acting on it as well as a photograph of a dropper line from an active mussel farm in comparison.

The interactions between offshore systems, whether floating or fixed, with wind, waves, and currents have been a subject of extensive research. Within a fixed frame of reference, an approximation approach known as the Morison (1950) equation, which is an industry standard, has been widely employed to calculate the loads experienced by slender structures when exposed to waves and currents (DNV 2010). In particular, the hydrodynamic forces that waves exert on bivalves have attracted significant attention in various engineering applications, from the design and operation of farming systems (Dalton et al. 2019; Heasman et al. 2021; Landmann et al. 2021b) over the determination of the added forces by marine growth (Gansel et al. 2015; Nobakht-Kolur et al. 2021a, b) to the load analysis of fixed structures regard-
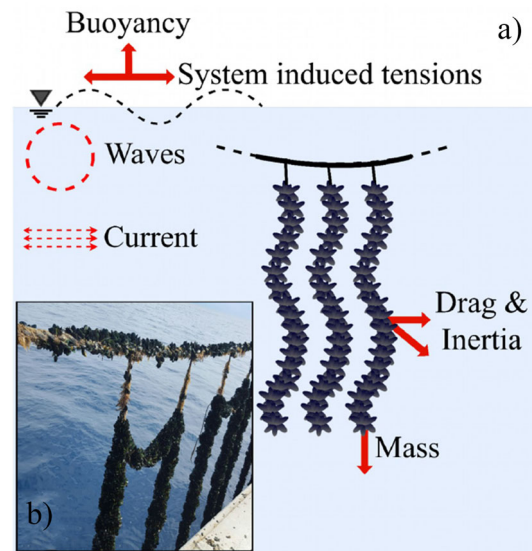

Fig. 1 Schematic sketch of a cultivation system for mussel and shellfish, with **a** dropper line suspended from a single backbone with environmental ocean parameters influencing it **b** and a photograph of a real-life example, where each loop is suspended for 5.0–10.0 m into the water column

ing added roughness through bivalve growth (Theophahatos 1988; Wolfram and Theophanatos 1990). Bivalve aquaculture facilities have undergone comprehensive examination utilizing theoretical, physical, and numerical methodologies, with a predominant emphasis on investigating the dynamics of fluid–structure interaction. Plew et al. (2005) detail the hydrodynamic implications of offshore bivalve farms based on observations and scaling arguments; they highlight the frequency-dependent wave attenuation caused by large farm setups. They draw comparisons between aquaculture installations and porous barriers, which reduce the water velocity with a first-order estimate of energy loss from currents. In a review by Stevens et al. (2008), the physics of open-water shellfish aquaculture are discussed regarding the effect of waves and currents on the farm systems. These authors conclude that a profound comprehension of system mechanics is indispensable for an accurate prediction of the hydrodynamic response and to avoid over-engineering during the design stages. In a study by Zhao et al. (2019), the hydrodynamic response of a longline system with lantern nets was considered in physical experiments, and their results suggest that especially the wave period needs to be considered during the design of aquaculture facilities. A numerical model of a bivalve system was developed by Cheng et al. (2020), who focused on the flexibility of the suspended crop. The simplified, coupled dynamics model is used to calculate the dynamic response of the dropper lines within the aquaculture system. In another numerical study, the influence of a shellfish structure on the passing water is investigated in a 2D computational fluid dynamics model (Delaux et al.

(2010)). The wake phenomena demonstrate that the drag exerted by the longlines on the fluid in motion leads to energy dissipation, causing a decline in the average flow velocity. The study utilizes a drag coefficient sourced from existing literature. The wave attenuation potential of aquaculture farms with suspended canopies, i.e., longline systems, was studied by Zhu et al. (2020) to show that these system can be used as nature-based coastal protection. They formulated a frequency-dependent theoretical framework to describe the attenuation of waves by submerged and suspended canopies, subsequently corroborating its accuracy through experimental data collected in laboratory and field settings. Hydrodynamic coefficients were assumed based on literature. Knysh et al. (2020) modeled a submerged longline system with protective sleeves numerically, using the mechanistic fluid–structure interaction modeling software Hydro-FE (Fredriksson et al. 2003; Tsukrov et al. 2000) to predict the dynamic response of several system components. Their simulations provide estimates of the anchoring forces, mooring line tensions, and time series data on the motion of the mussel dropper lines. However, the data is not validated by physical experiments. Wang et al. (2022) used a numerical model to predict the forces acting on the nets in traditional fish cages and offshore fish farms. They concluded that their approach is superior to previously used screen force models for the simulation of the drag forces on and the velocity reduction behind aquaculture nets.

Nevertheless, the influence of waves on mussel dropper lines and their corresponding hydrodynamic behavior has been the subject of limited scientific inquiry. Plew et al. (2009) conducted drag measurements on an artificial mussel dropper line to determine whether in- and exhaling jets of mussels during their feeding action has a detectable influence on the drag coefficient. No discernible influence of the in- and exhalant jets was determined, and this observation was ascribed to the dropper line acting as a bluff body, primarily characterized by drag generated from pressure imbalances arising due to flow separation. In a computational fluid dynamics approach by Xu et al. (2020), the drag and wake effects of longline mussel dropper lines under tidal currents are studies numerically. Two numerical models based on the geometry of real mussel dropper lines are implemented and drag coefficients from C_D=1.1 to 1.2 at sub-critical Reynolds numbers are determined. The examination of the existing literature pertaining to the interaction of shellfish and fluid flow predominately discloses that previous investigations regarding the hydrodynamic coefficients of mussel dropper lines have been predominantly confined to scenarios characterized by uniform flow conditions. Drag coefficients have generally received attention, either through numerical simulations or physical experiments using uniform flow conditions. However, Gagnon (2019) summarizes that the hydrodynamic coefficients of mussel dropper lines (drag,

inertia and/or lift) in waves are still mostly unexplored. Aside from the lack of knowledge regarding oscillatory flows, it is evident that the flexibility and deflection of shellfish ropes subjected to environmental flow forces have been mostly overlooked. It is noteworthy that the motion of the rope itself alters the velocity and acceleration data crucial for deriving meaningful outcomes using the Morison equation (1950), which relies on these parameters as input.

A first set of physical experiments in regard to the response of shellfish-encrusted rope with respect to oscillatory flows has been conducted (Landmann et al. 2021a), yet their parameter range for the dimensionless Keulegan–Carpenter number $KC = \frac{u \cdot T}{D}$ covered was limited due to the scale of the research facility (KC $\leq$ 10). Generally, the KC number describes the relative importance of the drag forces over inertia forces in an oscillatory flow, where u is the water particle velocity, D is the characteristic diameter of the observed object, T is the wave period. Gieschen et al. (2020) conducted large-scale experiments on mussel dropper lines under oscillatory flow covering a wider KC range from KC = 10–90. However, due to relative horizontal motion of the dropper lines, further enhancement of the evaluation method appears to be required for a more precise estimation of the hydrodynamic coefficients. Especially the inertia coefficients of mussel dropper lines under waves has not been sufficiently determined before. Currently used comparisons to marine roughened cylinders (Wolfram and Theophanatos 1990) are likely not applicable as they do not account for flexibility and porosity of specimen, as do the tests conducted here.

To address the existing deficiencies in current research and enhance the accuracy of hydrodynamic coefficient estimations pertinent to marine conditions with shellfish-covered crop ropes, the primary aim of this investigation is to design a numerical model. This model is employed to examine the hydrodynamic coefficients of mussel dropper lines, utilizing data obtained from a large-scale physical experiment. Based on a comprehensive physical data set the paper addresses the creation of a new numerical model approach in regard to the forces involved in mussel aquaculture, extending the applicability to different wave conditions, and providing practical recommendations for drag and inertia coefficients. These additions collectively contribute to a more holistic and applicable understanding of the hydrodynamics of mussel dropper lines.

To this end, the specific objectives within this study are:

- to separate the complex interdependent loads a mussel dropper is subjected to,
- to gain insight into the hydrodynamics based on large-scale laboratory tests,
- to develop and validate a suitable numerical model, able to accurately predict forces on and motions of dropper lines in oscillatory flows based on the Morison (1950)

equation. The equation is modified to better represent the forces acting on mussel dropper lines under oscillatory flow conditions by incorporating motion of the observed structure,

- to evaluate, assess, and report on the hydrodynamic coefficients of mussel dropper lines and a surrogate structure for KC numbers up to $\sim$ 90, while taking response motion in the form of line deflection into account.
- to discuss the appropriateness of the developed model in regard to longline aquaculture, the importance of the characteristic diameter and the influence of the overall dropper line length on the force evolution.

In this study, we aim to highlight a relatively unexplored facet of aquaculture engineering, introducing a novel numerical approach that explores the interplay between flow dynamics and structural motion. It is noteworthy that, in the realm of aquaculture, there has been a scarcity of investigations that focus on the relative velocity and acceleration between the flow and the motion of structural components. By emphasizing this aspect, we aim to underscore the novelty of our work and its potential to significantly advance the understanding of hydrodynamic phenomena in the context of aquaculture systems.

2 Methods and methodology

2.1 Experimental setup

To understand the complex loading of mussel dropper lines exposed to oceanic conditions, using pre-tensioned crop rope to study the response with horizontal deflection by an oscillatory flow, a comprehensive set of experiments with live-mussel dropper lines as well as surrogate geometries was carried out at the Large Wave Flume (GWK), a joint institution of Leibniz Universität Hannover, Germany and Technische Universität Braunschweig, Germany. The GWK is 300 m long, 5.0 m wide and 7.0 m deep; its walls and bottom are made of cement plaster and smooth floating screed, respectively. The hydraulically driven wave machine 900.0 kW gives a maximum stroke of ± 4.0 m to the wave paddle, generating waves up to a height of 2.0 m. The opposite end has a wave absorbing beach wedge made of coarse gravel, at a slope of 1:6. The water depth was set to a constant 3.5 m during testing. The test location within the wave flume was positioned at a distance of about 100.0 m from the wave maker. A top and side view of the GWK wave tank with the locations of the installed instrumentation is presented in Fig. 2.

For the tests six dropper line specimens, farmed blue mussels (*Mytilus edulis*) from the Baltic Sea, as well as a surrogate dropper line were prepared. The derivation process of the sur-

rogate included sophisticated laser scanning, data modeling and curation, as well as laser-supported 3D-printing. A more detailed description of the surrogate in general, including their designing and manufacturing process, is reported elsewhere (Landmann et al. 2019). In summary, the surrogate was created based on the aforementioned 3D scanning, and the derivation process used the Abbott–Firestone approach (Abbott and Firestone 1933) for live to surrogate model conversion, as well as statistical mean value analysis. To that end, length, volume, weight, and width of a representative number of sample blue mussel shells were taken, and a digital average representation of blue mussel shells was developed with computer-aided design. The average model of the blue mussel shells was then arranged around a core cylinder (depicting a rope in size/diameter), by varying each shell's rotation randomly. The distribution was modeled according to the mean Abbot–Firestone curve determined through the 3D-scanning. A satisfactory behavior under oscillatory flow for low KC-numbers has already been proven (Landmann et al. 2021a).

For the tests, the live blue mussel dropper lines, and the surrogate, with a length of 2.0 m each, were mounted to stainless steel wires connected to a concrete block at the bottom and a steel beam at the top of the flume in a distance of approximately 100.0 m from the wave machine. 16 surrogate bodies with a height of 0.12 m each were added to a stainless steel rope and fixated using grub screws to prevent rotation to form the 2.0 m long surrogate dropper line. The stainless-steel wire rope had a diameter of 0.04 m and a maximum load of 1.56 kN (DIN-EN:12385-4:2008-06 2008). Force transducers (CTL100, XSENSOR, Darmstadt, Germany) were attached to the top and the bottom of each dropper line recording the wave-induced loads in x- (direction of wave travel) and y- (wall to wall of flume) direction. The forces in the z-direction (bottom to top of flume) were recorded with an additional inline force transducer (U2B, HBM, Darmstadt, Germany). Incident wave conditions were measured by capacitive wave gages (WG). The WGs, built in-house, include two electrodes, a measuring wire and a ground plane. The wave gages were located approximately 50.0 m before and after the installed dropper lines to record the incident (1–4) and transmitted wave conditions (WG 5–8). Furthermore, two WGs alongside four inductive current meters (SM-2001F, hs engineers, Hannover, Germany) were installed in a distance of 0.2 m and 2.9 m from the dropper lines. The SM-2001F are capable of tracking the water particle velocity in x-, y- and z-direction. The inductive current meters (ICMs) were positioned at depths of 1.0 m and 2.5 m below the still water line to provide information on the wave kinematics. In Fig. 3, a cross section at the position of the dropper lines (a) as well as a photography with the force transducers and the connecting wire in place (b) is depicted. Details regarding the capabilities of the instruments used are available in Table 1. More information regarding the
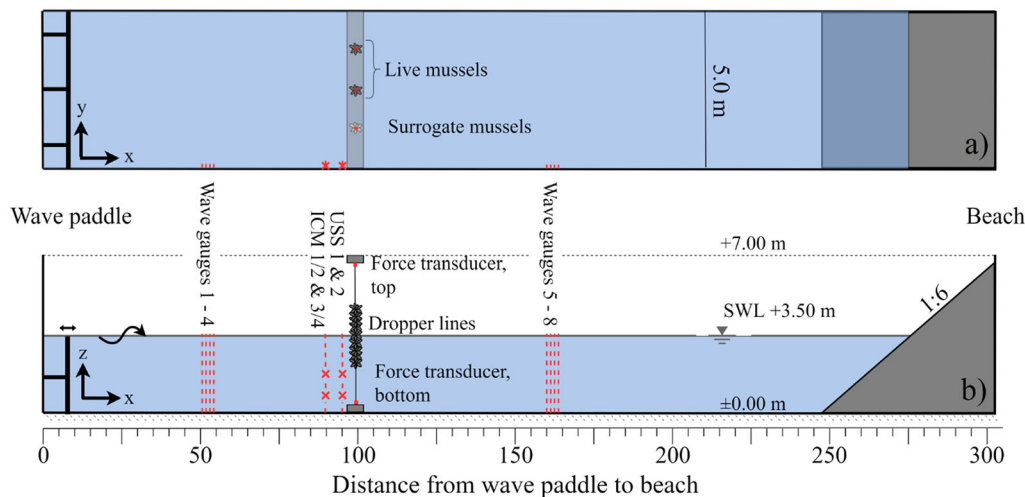
Fig. 2 **a** Top and **b** side view of the large wave flume with instrumentation and location of the dropper lines indicated. Not to scale

test setup, the adhesive strength of the byssus fiber and additional information on the biological properties of the mussel species is available in Gieschen et al. (2020).

The dropper lines were subjected to 13 different wave conditions with waves heights between 0.2m and 1.0 m and wave periods between 2.0s and 8.0s. They were chosen as a scaled example for the purposes of our study. We aimed to provide a baseline assessment to demonstrate the feasibility of longlines in a controlled and less extreme offshore environment. The authors acknowledge that these conditions do not fully represent real offshore sea states, particularly those with significant wave heights ($H < 6m$), which are more characteristic of actual offshore environments, but due to limitations in flume size these conditions could not be recreated in a 1:1 scale. The wave conditions are summarized in Table 2.

2.2 Physical model approach

Morison et al. (1950) proposed an empirical method to determine the wave force on a slender body ($\frac{D}{L} < 0.2$), e.g., the suspended mussel dropper lines. In that approach, the hydrodynamic pressure field and horizontal components of water particle velocity and acceleration for a given wave theory, which is dependent on the site-specific wave parameters, are identified and incorporated into the Morison (1950) equation where nonlinear drag forces F_D and inertia forces F_M are superimposed. This can be depicted as:

$$F = F_D + F_M = \frac{1}{2}\rho C_D u^2 A + \rho C_M V \dot{u} \qquad (1)$$

where F is the total horizontal force, ρ is the density of the water, C_D is the drag coefficient, u is the horizontal particle velocity, A is the referential area in flow, C_D is the inertia coefficient, V is the volume of the structure and $\dot{u}$ is the hor-

izontal particle acceleration. The hydromechanic drag C_D and inertia C_M coefficients found in Eq. 1 are empirical values used to quantify various parameters related to the shape of the investigated structure, its surface roughness, and the site-specific wave properties. These coefficients are usually determined experimentally.

The water particle velocity and acceleration needed to solve the Morison (1950) equation are determined according to their explicit wave theories (e.g., Airy, Stokes, stream function or cnoidal theory), These wave theories are based on different idealized boundary conditions and provide approximations of varying accuracy. Nevertheless, these theories provide good results, in particular for two-dimensional case studies. These monochromatic wave parameters are commonly used for practical engineering questions. More information regarding the fundamental formulations is gathered, compiled and available from several textbooks, providing further information and covering a broader scope than this study (Clauss et al. 1992, 1994; Dean and Dalrymple 1991; Holthuijsen 2007; Mèhautè 1976). To enable a comparison of the flow processes for various scales and fluid characteristics, the geometric similarity of the object in flow and their boundary limits need to be established. Furthermore, the acting forces in the flow system must be in a fixed relationship to one another at any point in time. In oscillatory flow, the non-dimensional Keulegan–Carpenter number, introduced above, is used to allow for a comparison. It describes the relative importance of the drag forces over inertia forces in an oscillatory flow.

Equation 1 can be solved with the hydrodynamic coefficients as unknown variables while velocity and acceleration of the water particles fluctuate under the orbital motion of the waves. In this regard, the least-squares method (Raed and Guedes Soares 2018; Wolfram and Naghipour 1999;
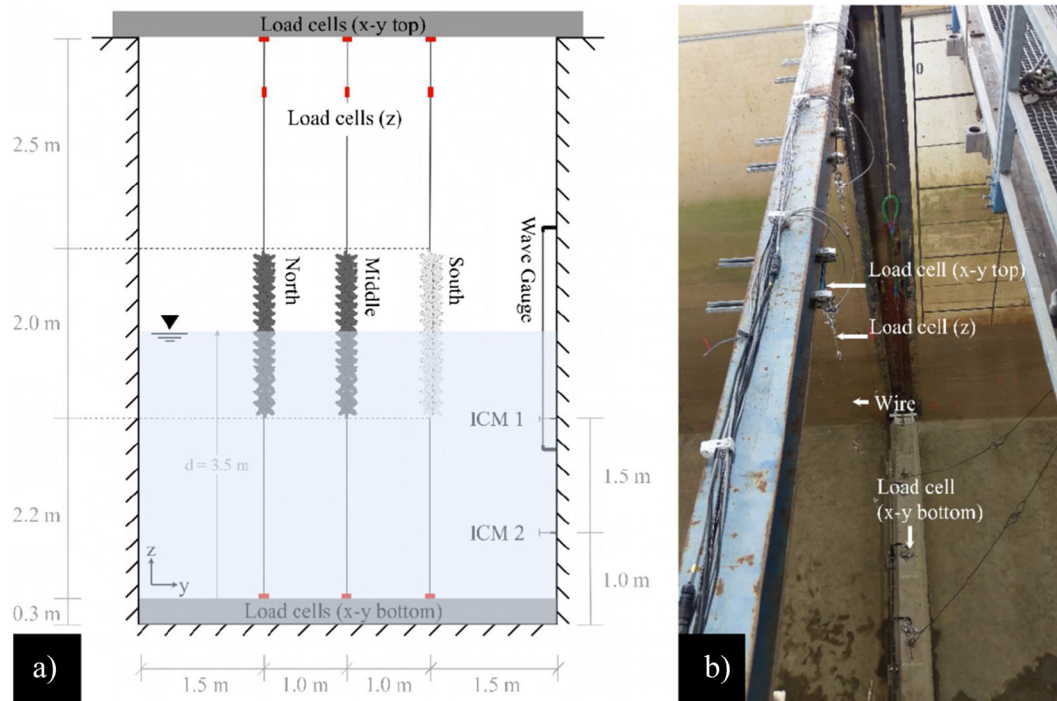
Fig. 3 **a** Cross section at the location of the physical model tests with instrumentation in place and **b** photography of the same location within the large wave flume

Table 1 Instrumentation

Instrument	Measurement range	Accuracy	Sampling rate
CTL1	0–1000 N	±0.2 N	1000 Hz
U2B	0–2000 N	±2.0 N	1000 Hz
Wave gage (in house)	–	±1 mm	100 Hz
SM-2001F	3 m/s	0.5% reading + 0.5% limit range	100 Hz

Bryndum et al. 1992) is seen as a standard approach in regression analysis to approximate the solution of overdetermined systems. It compares theoretically determined and experimentally measured forces, and then optimizes for the errors between those by using the least-squares method iteratively. The theoretical force is calculated based on the water elevation determined by the appropriate wave theory (cp. Table 2).

This study's wave test data were prepared using a fourth-order, low-pass Butterworth filter with a cut-off frequency of 3 Hz to eliminate frequency components associated with signal noise. Starting and end points of the data records were set by identifying the target wave height after ramp-up of the wave maker. Each wave between these points is identified individually via the zero-downcrossing method and the wave height, period, and length were detected.

For the determination of the theoretical forces, Stokes 2nd and 3rd order wave theory, according to Le Méhauté's diagram, were found to be a good approximation. We acknowledge the limitations of the Stokes wave theories in comparison to higher-order stream functions. Stokes wave theory was chosen for its simplicity and computational efficiency, especially in scenarios where wave heights are relatively small compared to the water depth, which applies to the offshore setting in which the prospective aquaculture farms are to be used. This choice allowed us to strike a balance between accuracy and computational tractability, which is often a practical necessity in engineering and numerical modeling applications.

Subsequently, the horizontal velocity $u(t, d)$ and acceleration $\dot{u}(t, d)$ of the water particles were calculated for each time step over the depth of the water column. The results were used to determine the theoretical forces for the wetted perimeter and submergence of the dropper line according to the Morison (1950) equation with varying C_D and C_M between 0.01 and 2.0. Thus, the theoretical horizontal loading on the dropper lines could be estimated as a function of the drag and inertia coefficients and the smallest mathematical error between the measured and theoretical value was used as an approximation of C_D and C_M. The KC number is used

Table 2 Wave parameters tested in physical experiments

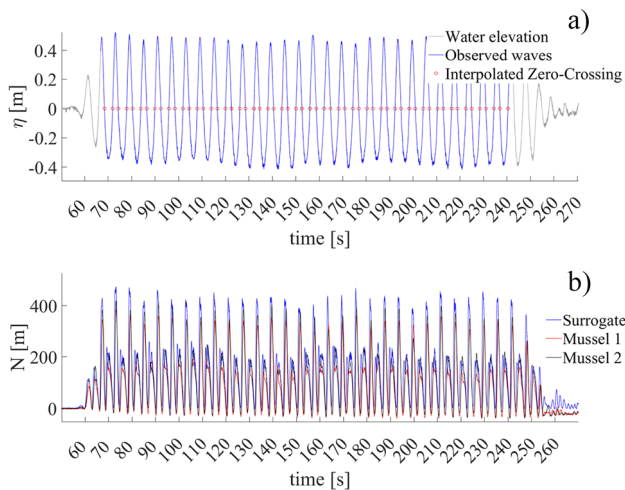| Wave ID [–]	Water depth [m]	Wave height [m]	Wave period [s]	Wave length [m]	Horizontal particle velocity [m/s]	KC-number [–]
1	3.5	0.2	2.0	6.23	0.31	5
2			2.5	9.56	0.25	5
3		0.4	3.0	13.10	0.45	11
4			3.5	16.60	0.42	12
5			4.0	19.99	0.41	13
6		0.6	4.5	23.30	0.62	23
7			5.0	26.53	0.62	26
8			5.5	29.71	0.63	28
9		0.8	6.0	32.86	0.89	44
10			6.5	35.96	0.91	49
11			7.0	39.04	0.94	54
12		1.0	7.5	42.11	1.29	80
13			8.0	45.15	1.33	89

Fig. 4 Time histories for a wave height of 0.8 m and a wave period of 6.0; **a** water surface elevation and **b** resulting forces. The observed time series as well as all interpolated zero-crossings are highlighted

as a reference, as it captures the variation in the measured drag and inertia coefficients.

Figure 4 shows time histories of water surface elevation and resulting horizontal total force of an exemplary measurement with a wave height of 0.8 m and a wave period of 6.0 s. The observed time series, within the total record period, as well as all interpolated zero-crossings are highlighted. The forces for the surrogate structure as well as the live mussels are shown to confirm the similar hydrodynamic behavior observed before (Landmann et al. 2021a).

2.3 Numerical model approach

For the numerical model, the stress-deformation behavior of the mussel dropper lines is modeled applying nonlinear

finite element analysis. The dynamic behavior of a dropper line encrusted with shellfish, following Huu-Tai and Seung-Eock (2011), may be described by employing rope elements undergoing large displacements, see Argyris and Scharpf (1972); Gambhir and Batchelor (1978), introducing masses and working surfaces of the rope as well as of the mussels. Damping is taken into account by Rayleigh damping, pre-stressing is incorporated later on by S_v but is not to be taken into account at the local formulation of equilibrium. The course of the rope is assumed to be linear between the nodes, such that no curvatures arise but sharp kinks at the computational nodes. Bending stiffness of the rope is neglected, external actions due to various forces are related to the nodes. The material behavior is estimated to be linearly elastic and strains are assumed to remain small. The geometry of the pre-stressed structure defines the initial configuration. Therefore, the respective local differential equation of motion, as per Dinkler (2020), reads:

$$\rho \frac{\pi D^2}{4} \dot{u}_{rs} + d_u u_{rs} + N_{,s} + p_s = 0 \qquad (2)$$

with the acceleration $\dot{u}_{rs}$ of the rope, the external damping characteristic d_u, the velocity u_{rs}, the longitudinal force N in direction of the rope, and external actions p_s which will be suitably distributed at discretisation. The equation is arranged in the updated position out of alignment. Additionally the Neumann boundary conditions are to be fulfilled with

$$m \dot{u}_{rs} + N - \bar{N}(t) = 0 \qquad (3)$$

whereby $\bar{N}(t)$ indicates the respective component of the external actions affecting the respective element of the rope

being under consideration. Dead load, buoyancy, and hydrodynamic loads are taken into account.

The updated force components of element i related to the global direction j may be computed to

$$s_{i,j} = (S_{v,i} + N_i) \frac{\Delta x_{i,j} + \Delta w_{i,j}}{l_i} \tag{4}$$

with the chosen pre-stress $S_{v,i}$ and the material equation

$$N_i = EA \cdot \varepsilon_i + \eta_k A \dot{\varepsilon}_i \quad \text{with} \quad \varepsilon_i = \frac{l_i - l_{v,i}}{l_{0,i}} \tag{5}$$

describing the rope force N_i due to external action and dynamic excitation in updated longitudinal direction of the rope element i with the constant longitudinal strain ε_i inside the element and the Kelvin–Voigt damping characteristic $\eta_k A$. The updated length of the rope element l_i, the pre-stressed length of the rope element $l_{v,i}$ as well as the original length without pre-stressing $l_{0,i}$ are given with

$$l_i = \sqrt{\sum_j \left(\Delta x_{i,j} + \Delta w_{i,j} \right)^2}, \quad l_{v,i} = \sqrt{\sum_j \left(x_{bi,j}^0 - x_{ai,j}^0 \right)^2},$$

$$l_{0,i} = \frac{l_{v,i}}{1 + \frac{S_{v,i}}{EA}}. \tag{6}$$

E indicates the Young's modulus and A is the cross-sectional area. The original nodal coordinates $x_{i,j}^0$ related to element nodes (a) and (b) of the pre-stressed rope are employed such as the unknown displacement components $w_{i,j}$. Symbol Δ indicates the difference evaluated from the values at nodes (a) and (b).

Global equilibrium is enforced weakly by applying the principle of virtual displacements and employing linear shape functions to describe the global displacement components related to directions $j = 1, 2, 3$ as well as the respective linearly independent virtual displacements. A multiplicative approach employs the spatial shape functions $\boldsymbol{\Omega}$ and the time-dependent amplitudes of nodal displacements $\boldsymbol{v}_j(t)$, velocities $\dot{\boldsymbol{v}}_j(t)$ and accelerations $\ddot{\boldsymbol{v}}_j(t)$ (Dinkler 2020),

$$w_j(x_j, t) = \boldsymbol{\Omega}(x_j) \cdot \boldsymbol{v}_j(t), \tag{7}$$

$$u_{rj}(x_j, t) = \boldsymbol{\Omega}(x_j) \cdot \dot{\boldsymbol{v}}_j(t), \tag{8}$$

$$\dot{u}_{rj}(x_j, t) = \boldsymbol{\Omega}(x_j) \cdot \ddot{\boldsymbol{v}}_j(t). \tag{9}$$

Introducing the approach into the work equation gives

$$\delta A = \delta \boldsymbol{v}^T \left\{ -\int \boldsymbol{\Omega}^T \rho \frac{\pi D^2}{4} \boldsymbol{\Omega} \, \mathrm{d}x \, \ddot{\boldsymbol{v}} - \int \boldsymbol{\Omega}^T \mathrm{d}_u \boldsymbol{\Omega} \, dx \, \dot{\boldsymbol{v}} - \int \boldsymbol{\Omega}_{,x}^T \boldsymbol{s} \, \mathrm{d}x \, \boldsymbol{v} \right. \tag{10}$$

$$\left. + \int \boldsymbol{\Omega}^T \boldsymbol{p} \, \mathrm{d}x + (\boldsymbol{\Omega}^T \bar{N})|_{bound} \right\} = 0. \tag{11}$$

Finally, matrix–vector notation yields

$$\boldsymbol{M} \cdot \ddot{\boldsymbol{v}} + \boldsymbol{D} \cdot \dot{\boldsymbol{v}} + \boldsymbol{K} \cdot \boldsymbol{v} - \boldsymbol{p} = 0. \tag{12}$$

The dropper lines are excited by horizontal hydrodynamic loads provided by evaluation of the modified Morison equation, compare Eq. (1), extending it to moving structures

$$f_{\mathrm{mod}}(t, z) = f_{\mathrm{D,mod}}(t, z) + f_{\mathrm{M,mod}}(t, z) \tag{13}$$

$$= \frac{1}{2} C_{\mathrm{D}} \rho D (u_{\mathrm{w}} - u_{\mathrm{r}}) |u_{\mathrm{w}} - u_{\mathrm{r}}| + C_{\mathrm{M}} \rho \frac{\pi D^2}{4} (\dot{u}_{\mathrm{w}} - \dot{u}_{\mathrm{r}}) \tag{14}$$

with f_{mod} being the horizontal force component depending on time t and vertical ordinate z, u_{w} being the horizontal velocity of the water related to the horizontal velocity of the rope u_{r}, and $\dot{u}_{\mathrm{w}}$ being the horizontal acceleration of the water related to the horizontal acceleration of the rope $\dot{u}_{\mathrm{r}}$. For clear representation, the ordinates t, z are omitted at all further representations concerning velocity as well as acceleration of the water. The wave characteristics, given by u_{w} and $\dot{u}_{\mathrm{w}}$, are taken from 3rd order wave theory (Stokes 2009) with

$$u_{\mathrm{w}} = c \cdot \left[k \cdot a \cdot \frac{\cosh[k(z+d)]}{\sinh(kd)} \cdot \cos(\Theta) \right. \tag{15}$$

$$+ \frac{3}{4} k^2 a^2 \frac{\cosh[2k(z+d)]}{\sinh^4(kd)} \cdot \cos(2\Theta) \tag{16}$$

$$\left. + \frac{3}{64} k^3 a^3 \cdot \frac{11 - 2\cosh(kd)}{\sinh^7(kd)} \cdot \cosh[3k(z+d)] \cdot \cos(3\Theta) \right] \tag{17}$$

and

$$\dot{u}_{\mathrm{w}} = c \cdot \left[k \cdot \omega \cdot a \frac{\cosh[k(z+d)]}{\sinh(kd)} \cdot \sin(\Theta) \right. \tag{18}$$

$$+ \frac{3}{2} k^2 \omega a^2 \cdot \frac{\cosh[2k(z+d)]}{\sinh^4(kd)} \cdot \sin(2\Theta) \tag{19}$$

$$\left. + \frac{9}{64} k^3 \omega a^4 \cdot \frac{11 - 2\cosh(2kd)}{\sinh^7(kd)} \cdot \cosh[3k(z+d)] \cdot \sinh(3\Theta) \right]. \tag{20}$$

The above equation uses $k = 2\pi/L$ as the wave number with L indicating the wave length, $\omega = 2\pi/T$ is the angular frequency with T indicating the wave period and $\Theta = kx - \omega t$ is the phase angle. The still water depth d and the amplitude a are determined by implicitly solving the equation

$$H = 2a + \frac{3}{32} \cdot k^2 a^3 \left[\frac{1 + 8\cosh^6(kd)}{\sinh^6(kd)} \right]. \tag{21}$$

Consequently, following the finite element procedure to take into account time as well as space variant dynamic excitation, the generalized α-method by Chung and Hulbert (1993), a generalization of the Newmark scheme is applied for time integration. The nonlinear system of equations is consistently linearized and solved by applying Newton–Raphson scheme.

Approaching the space variance of the loading terms, a polygonal shape is assumed over the height regarding the nodes of the mesh, and considering both situations either uncovered ropes or areas overgrown with mussels. Numerical integration yields terms either depending on the respective mass or on the respective working surface. Hence, terms related to the unknown nodal rope accelerations as well as to the unknown nodal rope velocities are introduced to the left hand side of the system of equations, whereby terms originating from the wave excitation itself are taken into account at the right hand side. The numerical damping control parameter ρ_∞ is chosen to be 1.0, compare Eq. (14) for all numerical analyses in this study. The Rayleigh damping parameters that are introduced into the generalized damping matrix

$$D = \alpha M + \beta K \tag{22}$$

are determined from experimental decay tests on the system as per Sect. 2.2 to $\alpha = 2e - 6$ and $\beta = 0.004$, respectively. The boundary conditions for the numerical model are depicted in Fig. 5. In all computational runs, the element size is chosen to 0.1 m. The water level at rest is equal to $x_3 = 0$, whereas all displacements are fixed at node a and b. In the red-colored sections, see Fig. 5, the mussels are present and the distribution of the orbital velocity is shown qualitatively over the depth of the water. Please note that the distribution varies in height due to wave characteristics.

3 Results

3.1 Numerical model for the determination of hydrodynamic loads on mussel dropper lines

The results of the developed numerical model, which is based on a modified Morison equation (cp. Eq. 14) are shown below. They are verified using the experimental data obtained in a large-scale wave tank as a comparison. Figure 6 shows time histories of surface elevation and horizontal forces, for four different sets of wave parameters, which together with the characteristic diameter of $D_{char} = 5.5$ cm, cover KC = 5 (Fig. 6a), KC = 13 (Fig. 6b), KC = 44 (Fig. 6c), and KC = 89 (Fig. 6d) (cp. Table 2). All displayed results are based on an unchanged set of hydrodynamic coefficients ($C_D = 1.1$, $C_M = 1.0$) to show the validity of the model for a large variety of conditions even without an individual adjustments of the force coefficients.

Generally, a very good agreement of the numerical and experimental results is found. The forces exerted by the experimental waves range from a minimum, that is equal to the pre-stressed tension of ~75 N, to a maximum of ~850 N. The force magnitudes appear consistent with available literature, as similar forces have been recorded by Gagnon and
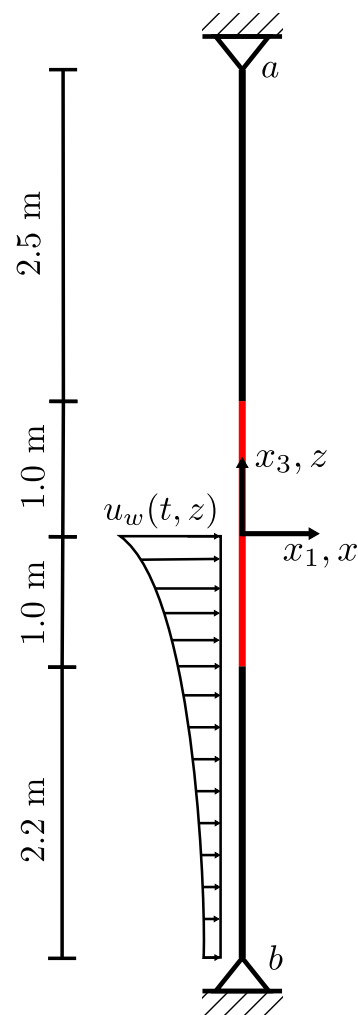

Fig. 5 Numerical model of dropper line—geometry and loading

Bergeron (2017) for dropper lines in observational studies of mussel farms. The forces in the numerical model similarly range from ~75 N to ~750 N. Nevertheless, the expected peak forces in the numerical model for lower KC ranges (5–13) are overestimated by up to 12.5%. For higher KC ranges (44–89), the expected peak forces in the numerical model are underestimated by up to 15%. Overall, the amplitudes of the inline forces agree well for all KC ranges. The phase difference between the physical and numerical model is small. For higher KC numbers, no difference can be detected (cp. Fig. 6d). Small orbital wave motions (cp. Fig. 6a) and waves with large amplitudes (cp. Fig. 6d) are well represented with the numerical model. The wave-induced force characteristics visible in the experimental data are also accurately reproduced by the numerical model.

For lower KC ranges, the cyclical excitation by the wave is well represented (cp. Fig. 6a) by the numerical model, indicating that wave phases are equally consistently predicted. For each wave cycle, the initial passing of the wave along the dropper line leads to a first force peak. From there, a

decrease in the water surface elevation of the wave corresponds to a simultaneous decrease in inline force. The wave trough coincides with a force minimum. The rising water elevation corresponds to a rise and second peak in inline forces. The directional shift in fluid motion coinciding with the wave peak leads to a second force minimum in inline forces. Overall, every second force peak is slightly lower than the first, which is also presented in the experimental data. This behavior is due to the momentum and added mass of the wave's water pulling on the dropper line. The flow regime at $KC = 5$ is inertia-dominated, i.e., the inertia force is mainly responsible for the overall forces. The inertia effects dominate viscous effects as the duration necessary to develop the boundary layer and flow separation can not be reached. This leads to a different force evolution compared to the other cases.

For higher KC ranges, (cp. Fig. 6b, c, d), a drag-dominated flow regime can be assumed. The drag force is not synchronous with the inertia force, which is why the different force evolution can be observed. Here, a first load peak is reached when the wave crest reaches the dropper line, i.e., the horizontal motion of the water particles at the wave crest is at a maximum. The next load peak is reached when the wave trough passes the dropper line, again caused by the horizontal, albeit oppositely directed motion of the dropper line. This second peak is consistently smaller, as it describes a particle motion adverse to the direction the wave propagates. The force peaks induced by the incoming, first wave is especially pronounced in the experimental data, which is in good agreement with the data of the numerical model.

By applying the Morison (1950) equation to the dropper lines within the finite element procedure, some limitations become apparent. As the Morison equation simplifies the complex interactions between dropper lines and the surrounding fluid flow, hydrodynamic processes, such as vortex generation and shedding, are neglected. Their influences are only captured in the hydrodynamic coefficients of drag and inertia, in which the influences of several physical processes are compounded without distinction. For a differentiation between all influencing factors a fully integrated and coupled fluid dynamics approach would be necessary, which was not within the scope of this study.

3.2 Displacement of the mussel dropper lines under waves

Although the system is pre-stressed, experiments show horizontal displacements, that cannot be measured by the setup. However, the numerical model yields the horizontal displacements of the cable loaded by wave excitation and employing the same wave parameters as above. This is shown in Fig. 7, where a positive displacement is evaluated in the direction of the traveling wave, as indicated in Fig. 2 above. The computation of the displacement is needed for the correct

determination of the acting forces. For the smallest wave amplitude (cp. Fig. 7a), a continuous, persistent displacement pattern of the dropper line under the orbital wave motion can be observed. The dropper line is displaced by 0.03 m during the passing of a single wave, with amplitudes of ± 0.03 m. For larger waves, the amplitude of the horizontal displacement increases, but the displacement pattern is no longer harmonious. The displacement increases up to ± 0.16 m for the highest KC numbers (cp. Fig. 7d). The disharmonious displacement of the dropper line is due to the increasing drag forces induced by the passing waves.

The displacement is induced by the passing waves and slightly time-shifted in regard to the wave characteristics, i.e., the displacement maximum is reached shortly after the wave crest passed the dropper line. For the lowest KC ranges, the numerical model produces a cyclical displacement pattern (cp. Fig. 7a). Every wave crest and trough causes a displacement of the dropper line, which is counter-acted by the restoring forces. For higher KC numbers (cp. Fig. 7b), an irregular displacement pattern can be observed. During the zero-crossings of the water elevation, the horizontal force acting on the dropper line is minimal. But restoring forces occur at wave troughs and crests causing a sudden return to the initial position. This does not occur for even larger KC numbers (cp. Fig. 7c and d). Here the drag forces acting on the dropper line are larger than the restoring forces during the zero-crossings of the water elevation. This is supported by the observation that the positive displacement is larger, i.e., the dropper line is pulled in the direction of the traveling wave.

A comparison to visual data taken during the experiments shows slightly larger displacements for the experiments. This is due to the heterogeneous nature of the natural dropper lines, i.e., the mussel beset polyethylene line at the core. For the surrogate dropper line, with a continuous metal wire and uniformly spaced surrogate mussel nodes, the results are comparable to those evaluated by the numerical model.

3.3 Influence of modified Morison equation

The original Morison (1950) equation (cp. Eq. 1) was modified to account for the shown horizontal displacement and motion dynamics of the observed mussel dropper line (cp. Eq. 14). This is illustrated in Fig. 8, where the experimental results for the cable force are shown together with the numerical results for the original and modified Morison equation for the same wave parameters as above.

Apparently, the original Morison (1950) equation substantially overestimates the force evolution by up to 90%, when the exciting velocity and acceleration fields are not correctly used. This applies especially for peak loads, which amount to up to 950 N for the original Morison (1950) equation for $KC = 44$ (cp. Fig. 8c). The results of the experimental data
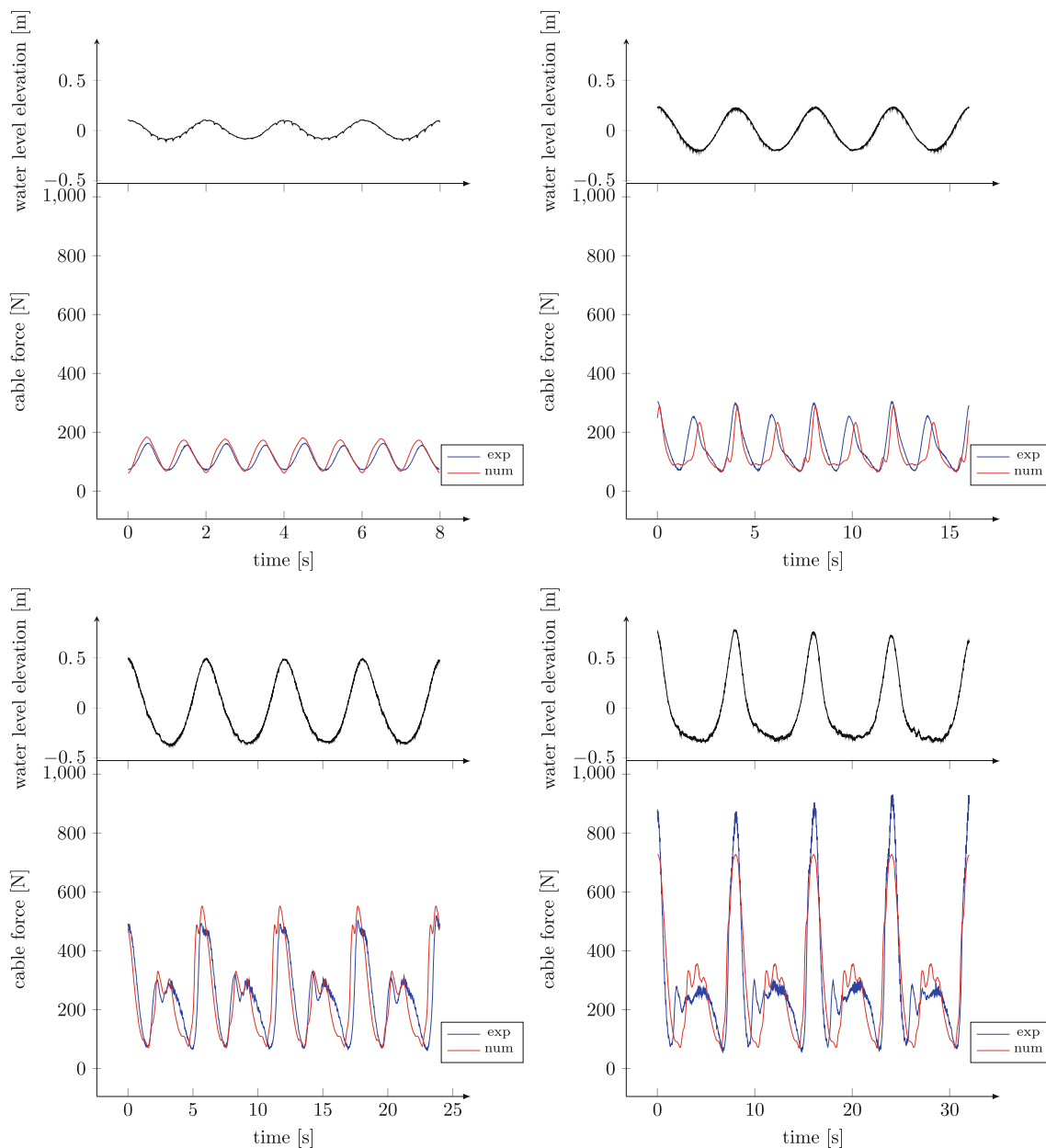
**Fig. 6** Time histories of water surface elevation and horizontal total forces at $z = 3.5$ m for Wave ID 1 [**a** $H = 0.2$ m, $T = 2.0$ s], Wave ID 5 [**b** $H = 0.4$ m, $T = 4.0$ s], Wave ID 9 [**c** $H = 0.6$ m, $T = 6.0$ s], Wave ID 13 [**d** $H = 1.0$ m, $T = 8.0$ s]

and the modified Morison equation for the same KC-number are significantly lower with 500 N and 550 N, respectively. Furthermore, the resulting force is phase-shifted and not aligned with the experimental data. The above described effects are caused by disregarding the displacement that the dropper line is experiencing as a result of the wave excitation, thus reducing the local relative fluid–structure velocity and acceleration.

The actual water elevation, displacement of the dropper line, and measured forces need to be accurately accounted for at the precise location in time and space to generate the correct results. This is why a generally poor agreement of

the original Morison (1950) equation (cp. Eq. 1) with the experimental results is determined for the whole KC-range. Especially for higher KC numbers, which coincide with more energetic waves, this becomes especially apparent. It can be seen that an incorporation of the displacement, i.e., the position of the structure and water elevation in time and space, is essential to achieve agreeable results. The modified Morison equation (cp. Eq. 14), as used in this work, achieves excellent agreement, given the complex setup and pre-stressed line configuration with non-uniformly distributed shellfish load.

In summary, contrary to the mainly observational and numerical approaches used to estimate forces on mussel
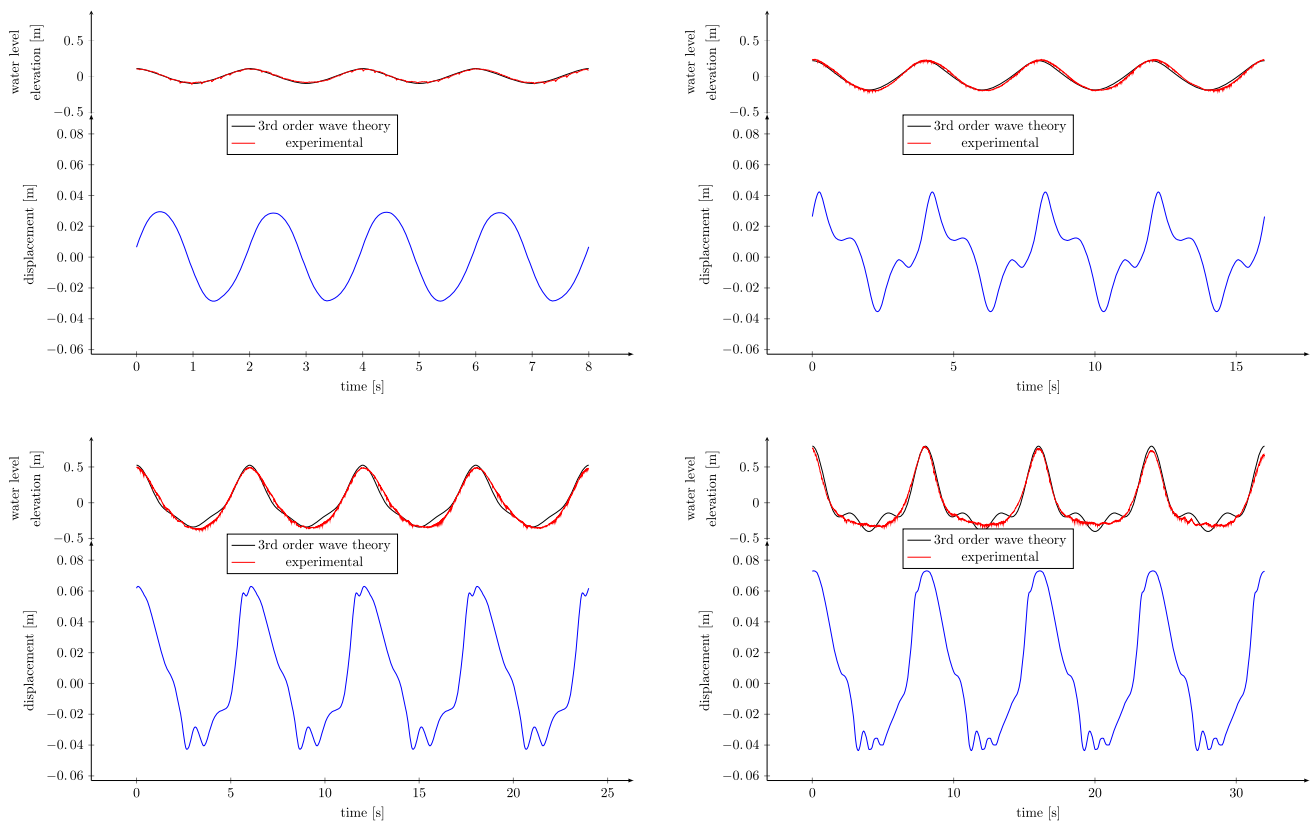
Fig. 7 Displacement of cable at $z = 0$ for Wave ID 1 [**a** $H = 0.2$ m, $T = 2.0$ s], Wave ID 5 [**b** $H = 0.4$ m, $T = 4.0$ s], Wave ID 9 [**c** $H = 0.6$ m, $T = 6.0$ s], Wave ID 13 [**d** $H = 1.0$ m, $T = 8.0$ s]

dropper line systems up to date, the depicted numerical model data, validated by experimentally determined data sets, now provide realistic results for the forces acting on mussel dropper lines. The comparison of experimental and numerical data shows that the numerical model is able to accurately capture the dynamic behavior of mussel dropper lines for a large parameter range. The displacement determined through the numerical model together with the modification of the Morison equation (cp. Eq. 1) allows the determination of forces of a natural and hard to capture system.

4 Discussion

4.1 Hydrodynamic coefficients

Using the numerical model, new insights regarding the hydrodynamic coefficients can be obtained. The determination of hydrodynamic coefficients for floating or fixed structures employed in the marine aquaculture industry is a frequent research topic (i.e., Stevens et al. 2008). Most recently, based on experiments in steady flow, a drag coefficient of $C_D = 1.6$ for blue mussels (*Mytilus edulis*) at sub-critical flow regimes ($Re < 10^5$) is recommended (Landmann et al. (2021a)). This drag coefficient matches

existing data while it expands on the range of previously assessed ranges of Reynolds numbers. Differences in results can mainly be attributed to differences in the approaches in the existing research. Raman-Nair and Colbourne (2003), Raman-Nair et al. (2008), and Knysh et al. (2020) based their reported drag coefficients on assumptions in relation with ultra-rough cylinders. Xu et al. (2020) conducted numerical experiments with mussel dropper lines without a validation through physical tests. Plew et al. (2005), Plew et al. (2009), and Gagnon and Bergeron (2017) conducted physical experiments with dropper lines. In these experiments, sources for the differences are biological, e.g., stage of mussel growth, mussel density along the length of the dropper line, the number of hitchhiker/fouling organisms on the mussel shell as well as the manner of data acquisition, e.g., through field experiments where parameters influencing the hydrodynamics can not be clearly differentiated. Regarding oscillatory flow, the hydrodynamic coefficients of mussel dropper lines have not been thoroughly determined before. Landmann et al. (2021a) determined for KC < 10 a drag coefficient of $C_D = 2.3$ and an inertia coefficient of $C_M = 2.1$ for blue mussels (*Mytilus edulis*). While this only covers a very limited range, it has been demonstrated that an experimental determination of the hydrodynamic coefficients of mussel dropper lines in oscillatory flow is however possible.
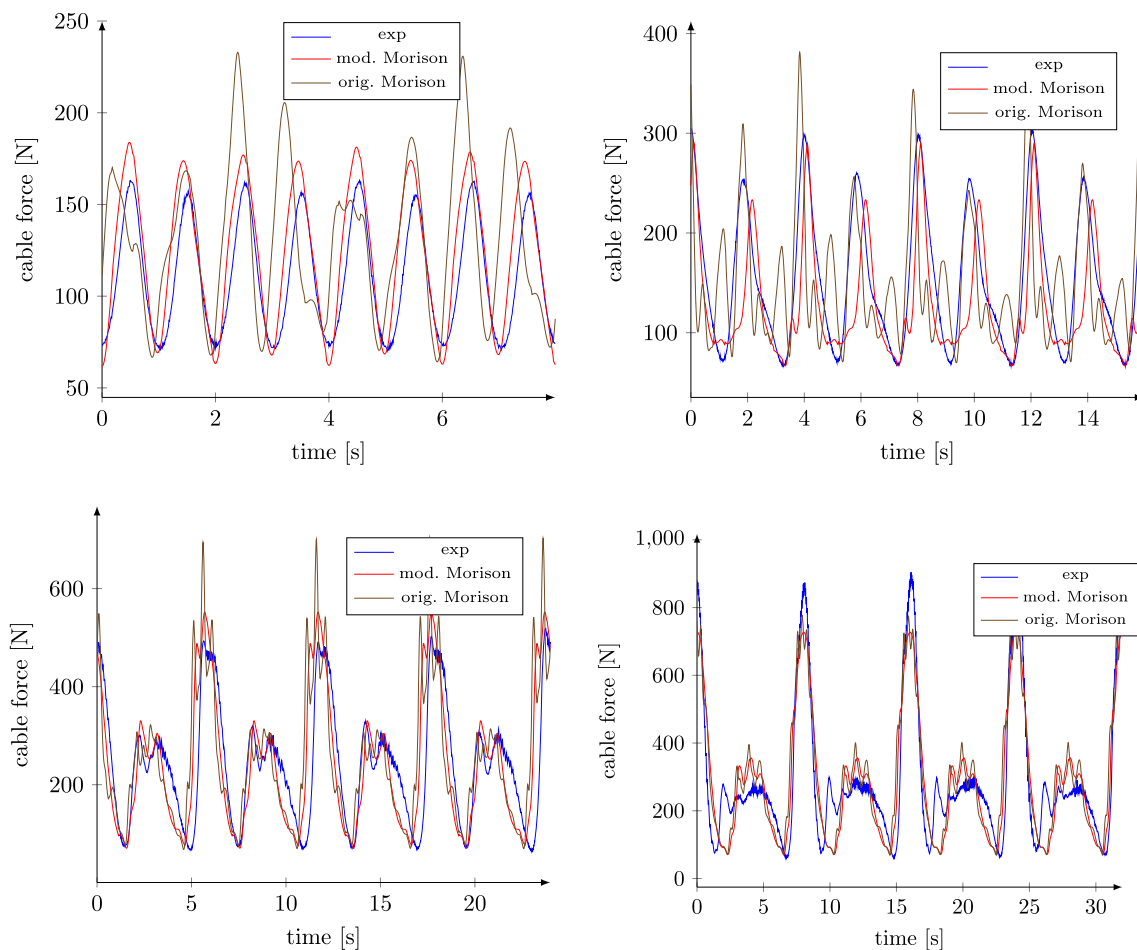
Fig. 8 Results of original and proposed modified Morison equation in comparison to experimental data for Wave ID 1 [**a** $H = 0.2$ m, $T = 2.0$ s], Wave ID 5 [**b** $H = 0.4$ m, $T = 4.0$ s], Wave ID 9 [**c** $H = 0.6$ m, $T = 6.0$ s], Wave ID 13 [**d** $H = 1.0$ m, $T = 8.0$ s]

In this work, large-scale tests with mussel dropper lines in oscillatory flow have been conducted for the first time. The obtained data, together with the numerical model, made the provision of hydrodynamic force coefficients for a more comprehensive range of KC numbers (23–90). Relying solely on the experimental data, limitations regarding a conclusive determination of the drag and inertia coefficients were encountered. These limitations arose from the inability to ascertain the displacement of the mussel dropper lines under wave load. Displacement measurements were not feasible as the visual access to the dropper line motion had been obstructed by highly opaque, sediment-rich water from a near-by shipping canal used in the large-scale facility. This has also been described by Gieschen et al. (2020). Using the developed numerical model, an average drag coefficient of $C_D = 1.1$ and an inertia coefficient of $C_M = 1.7$ are proposed for drag-dominated, oscillatory flow conditions for KC = 40–90, which were made possible through the inclusion of more accurate information on the relative velocity and acceleration in the frame of the affected dropper lines, and stretching the entire deflected length of the dropper. For

a general estimation for specific KC ranges, see the results presented in Fig. 9. The results for KC < 20 are not included, as the results for this inertia-dominated KC-regime are prone to fluctuations as the influence of the drag force is low. For this flow regime, the results from Landmann et al. (2021a) are applicable. For flow conditions between KC = 20–40, further testing is necessary to accurately separate drag and inertia components in oscillatory flow.

We acknowledge that a significant portion of practical applications involves KC numbers in the range from KC = 5–40. However, the physical model tests did not conclusively cover this range with wave parameters as the overarching aim of this study was to develop and validate a suitable numerical model, able to accurately predict forces on and motions of dropper lines in oscillatory flows based on the Morison (1950) equation. As the numerical model was employed to determine the drag and inertia coefficients, no variations of the results are captured as the input parameters regarding the force, characteristic diameter, flow velocity and acceleration were kept static. The practice of employing a constant and unchanging value for hydrodynamic coefficients across
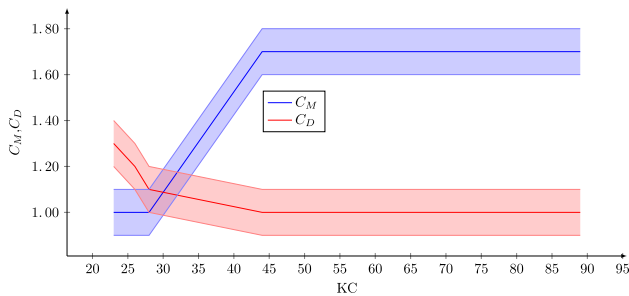
Fig. 9 Drag and Inertia coefficients for KC = 23–90 according to the numerical model with error envelope to account for variations and uncertainties in the hydrodynamic coefficients

all objects is a common simplification in modeling. However, it lacks realism. To address this limitation, we have included an error envelope in Fig. 9 to account for variations and uncertainties in the hydrodynamic coefficients, recognizing the need for a more realistic representation of these coefficients in practical applications.

4.2 Influence of the characteristic diameter

The characteristic diameter used for the calculation of hydrodynamic coefficients needs to be selected carefully Landmann et al. (2021b). In bivalve aquaculture, several approaches to determine the correct characteristic diameter exist according to Gagnon (2019). It is a challenging task since mussel dropper lines are natural structures with uneven growth, cavities, crevasses, and protrusions. They consist of hard growth composed of the mussels of varying sizes, overgrown with soft growth consisting of different algae, anemones, sponges, and kelp species. A schematic view of soft and hard growth on a dropper line is shown in Fig. 10. This visualizes the inherent difficulties in determining the correct characteristic dimensions of any object exposed to nature. Isbert et al. (2023) make a useful contribution in obtaining and sampling biofouled specimen in realistic environments and lay a sound basis for characterization of fouling communities and impact assessment.

The combined influence of soft and hard growth on dropper lines could not be experimentally explored in this project as this would have required a more careful rearing of the specimen and the involvement of marine biologists. With a mixture of soft and hard growth, the drag coefficient varies significantly from those with purely soft or hard growth. The soft growth likely has a large influence on the boundary layer development as shown by Schoefs et al. (2022). Experiments by Theophahatos (1988) showed that the drag coefficient under steady flow increased when soft growth was included. It was shown that it was about 1.4 times greater for fully kelp covered cylinders compared to cylinders fully covered with a single layer of mussels. The surface roughness increases as the outcropping mussels grow to a harvestable size. Fur-

thermore, the mass increases, which also results in a force increase. Simultaneously, the drag coefficient increases with the surface roughness and diameter and thus the drag loads on the structure become more influential. The increased roughness affects various aspects of the flow around the mussel dropper lines such as hydrodynamic instabilities, i.e., vortex shedding, the interaction of vortices, the separation angle, the turbulence level as well as the vortex strength. Therefore, it can be assumed that the increased drag of live mussels in steady-state experiments is due to an increase in dropper diameter caused by the additional soft growth and a larger roughness. This is supported by the results of Wolfram and Theophanatos (1990) regarding the effects of marine growth on cylinders as well as more recent numerical studies by Xu et al. (2020).

To further investigate the effect of the characteristic diameter, the numerical model can be adjusted to allow for the use of species specific diameters (*Mytilus edulis*, *Perna canaliculus*, *Mytilus galloprovincialis*, etc.). Blue mussels, as tested in this study, are a prime species used in aquaculture. Blue mussels have been proven to be reliable for industrial purposes due to their high economic value, a wide distributional pattern and their ability to withstand wide fluctuations in salinity, desiccation, temperature and oxygen levels (Gren et al. 2018; Petersen et al. 2014). However, other species like the green-lipped mussel (*Perna canaliculus*) or the Mediterranean mussel (*Mytilus galloprovincialis*) are also harvested in large quantities in aquaculture systems. While displaying similar characteristics, size differences are apparent.

The influence of these size differences is exemplary shown in Fig. 11, where the displacement and inline forces are displayed over the associated, theoretical surface elevation for a wave height of $H = 0.6$ m and a wave period of $T = 6.0$ s. In the numerical model the three different species are differentiated by their mass and diameter as input parameters. A mass of 5.0 kg/m and diameter of 0.075 m for the *Mytilus edulis* are assumed based on literature (Gosling 2008). This is similar to the validated numerical solution displayed above. For the *Mytilus galloprovincialis* an increase in mass to 10.0 kg/m and in diameter to 0.110 m is assumed based on literature (Babarro and Carrington 2013). The *Perna canaliculus* is assumed to have an even higher mass of 15.0 kg/m and an increased diameter of 0.135 m based on literature (Hickman 1979). The results demonstrate the influence of mass and diameter on the force evolution of mussel dropper lines. An increase in both parameters leads to larger displacements as well as increased forces. The displacement increases from max. 0.06 m for *Mytilus edulis* to 0.08 m for *Mytilus galloprovincialis* and to 0.09 m for *Perna canaliculus*. Similar increases are also visible for the exerted forces, with maxima for *Mytilus edulis* = 700 N, for *Mytilus galloprovincialis* = 950 N, and for *Perna canaliculus* = 1050 N. Using these

Fig. 10 Schematic view of soft and hard biofouling on a dropper line **a** with real-life examples of green-lipped mussels (*perna canaliculus*) ©Goseberg, N. **b** and blue mussels (*Mytilus edulis*) ©Landmann, J
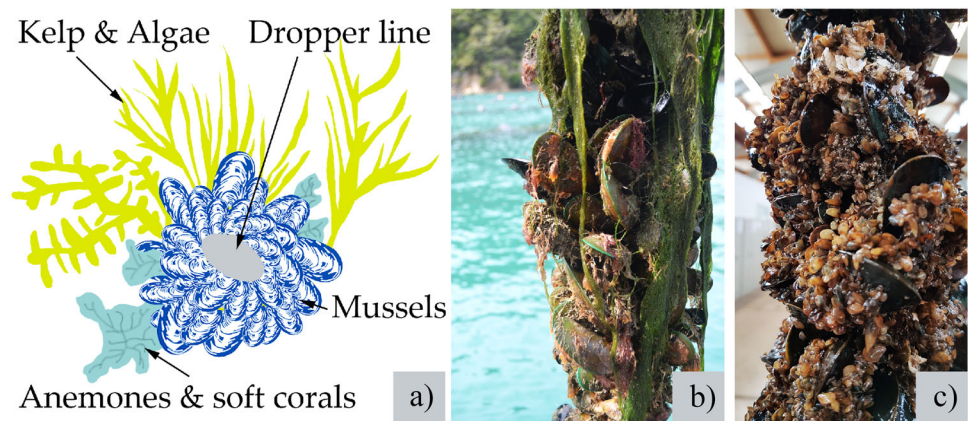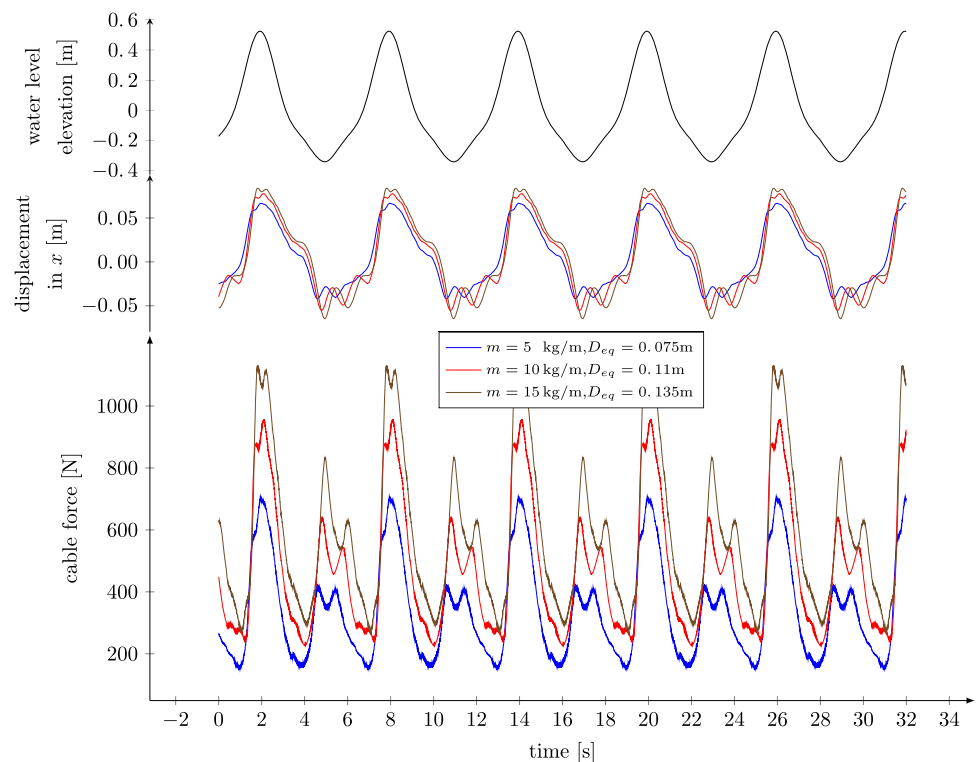

Fig. 11 Displacement–time–curve and force–time–curve for variation of mussel species using Wave ID 9 [**c** $H = 0.6$ m, $T = 6.0$ s] as example case

adjustments, a quick determination of the species-specific forces are possible.

Furthermore, applying the numerical model one can determine the occurring forces at any growth stage of the mussels. Especially in offshore environments this could prove to be advantageous, as buoyancy controlled farming systems are increasingly under consideration (Heasman et al. 2021). These systems can operate at varying depth, dependent on the overall buoyancy of the system. As an example, submergence of the system can be necessary to avoid forecasted extreme weather events. However, in this case, the station-keeping ability of these systems is of higher interest. By keeping the system and the mussels over their whole life cycle in an ideal growth zone within the water column the productivity of the whole farm can be increased (Avdelas et al. 2021). While the

determination of this position, based on oxygen level, light level, available food, etc., is a task for biologists, the numerical model can provide designers and engineers with valuable insights concerning the forces occurring in the whole system at varying life stages of the mussels. While forces at the spat-, and grow-out stage are expected to be minimal, an exact determination could lead to an optimisation of the current systems to avoid high load scenarios (Landmann et al. 2021b).

5 Conclusions

Considering the rapid growth of human population in coastal areas, coupled with sustainability and environmental concerns, underscores the pivotal role that bivalve aquaculture

can play in securing global food security. Additionally, this practice has the potential to offer substantial support for economic and social advancement. Importantly, sustainable bivalve aquaculture imposes significantly lower environmental costs and delivers increased benefits when compared to prevailing sources of animal protein. Based on this background, large-scale model tests are performed and an numerical model is developed and verified to predict the forces, that oscillating flow exerts on mussel dropper lines. Based on a modified Morison equation, which takes the movement of the slender body into account, the model accurately depicts the force evolution of mussel dropper lines under oscillatory flow. The numerical model incorporates wave–structure interaction of a dynamically moving multibody system. To the authors' knowledge, this is the first numerical model, validated by large-scale physical experiments, focusing solely on mussel dropper lines in oscillatory flow. The model allows the determination of the hydrodynamic drag and inertia coefficients and the displacement of the dropper line under waves. Furthermore, it can be used to gain insights into important secondary parameters such as the characteristic diameter. In conclusion, the research, presented here, allows for the quantification of the stresses of a single dropper line in oscillating flow. The main conclusions of this study can be summarized as follows:

- Using a large-scale laboratory mussel dropper lines are subjected to waves with varying parameters. The forces and hydrodynamic parameters are measured and numerically analyzed. Based on the results drag and inertia coefficients are determined for a large range of KC-numbers. A drag coefficient of $C_\mathrm{D} = 1.1$ and an inertia coefficient of $C_\mathrm{M} = 1.7$ are recommended to model shellfish-encrusted dropper lines exposed to oscillatory flows with KC = 40–90.
- A numerical model for the determination of wave-induced forces on mussel dropper lines is developed and validated using the experimental data. It employs a modified Morison equation, which takes into account the displacement of the mussel dropper line. The numerical model is able to accurately capture the dynamic behavior of mussel dropper lines for a large parameter range.
- The influence of varying aquaculture-related parameters is discussed by applying the numerical model, e.g., the characteristic diameter is varied. Based on the gathered insights, recommendations can be given from an engineering point of view concerning the optimal placement of mussel aquaculture within the water column.

Ultimately, these findings have the potential to assist researchers, policymakers, and industry leaders in developing, operating, and maintaining innovative marine aquaculture systems that align with the United Nations' Sustainable Development Goals. Given the ongoing population growth, urbanization of coastal areas, and increased demand for sustainable food sources, taking action in this domain is crucial.

The question of how to best utilize the presented research to achieve the most efficient aquaculture farm designs and systems is multifaceted and spans various scientific disciplines. Marine biologists can utilize this research to assess the extent and spatial scales of changes in water column processes (such as stratification, nutrient cycling, biodeposition, and resuspension). Ecologists can enhance their understanding of interactions within offshore aquaculture environments and the overall ecological impact of bivalve aquaculture. Engineers play a crucial role in designing and maintaining these systems and their components, ensuring their sustainability in highly energetic environments.

Safeguarding a sustainable food supply for future generations remains an ongoing and interdisciplinary research challenge, necessitating the expertise of offshore engineers to design, operate, and maintain critical systems. Future testing should investigate the specific influence of soft growth and surface roughness on the hydrodynamic parameters of mussel dropper lines. By applying the knowledge gained from this study to future research, this study establishes a numerical modeling basis for the evaluation of the displacements and forces involved in offshore bivalve aquaculture. The insights gathered in this study also facilitate the testing procedure for future aquaculture systems and provide robust estimates for numerical approaches.

Declarations

Conflict of interest The authors declare that they have no known competing financial interests or personal relationships that could have appeared to influence the work reported in this paper.

References

Abbott EJ, Firestone FA (1933) Specifying surface quality: a method based on accurate measurement and comparison. Mech Eng 55:569–572

Argyris J, Scharpf D (1972) Large deflection analysis of prestressed networks. J Struct Div 98(3):633–654

Avdelas L, Avdic-Mravlje E, Borges Marques AC, Cano S, Capelle JJ, Carvalho N, Cozzolino M, Dennis J, Ellis T, Fernandez Polanco JM, Guillen J (2021) The decline of mussel aquaculture in the European Union: causes, economic impacts and opportunities. Rev Aquac 13(1):91–118. https://doi.org/10.1111/raq.12465

Babarro JM, Carrington E (2013) Attachment strength of the mussel *Mytilus galloprovincialis*: effect of habitat and body size. J Exp Mar Biol Ecol 443:188–196. https://doi.org/10.1016/j.jembe.2013.02.035

Bryndum MB, Jacobsen V, Tsahalis DT (1992) Hydrodynamic forces on pipelines: model tests. J Offshore Mech Arct Eng 114(4):231–241. https://doi.org/10.1115/1.2919975

Buck BH (2007) Experimental trials on the feasibility of offshore seed production of the mussel *Mytilus edulis* in the German bight: installation, technical requirements and environmental conditions. Helgol Mar Res 61(2):87–101. https://doi.org/10.1007/s10152-006-0056-1

Buck BH, Langan R (2017) Aquaculture perspective of multi-use sites in the open ocean. Springer, Berlin. https://doi.org/10.1007/978-3-319-51159-7

Cheney D, Langan R, Heasman K, Friedman B, Davis J (2010) Shellfish culture in the open ocean: lessons learned for offshore expansion. Mar Technol Soc J 44(3):55–67. https://doi.org/10.4031/mtsj.44.3.6

Cheng W, Sun Z, Liang S, Liu B (2020) Numerical model of an aquaculture structure under oscillatory flow. Aquac Eng 89:102054. https://doi.org/10.1016/j.aquaeng.2020.102054

Chung J, Hulbert G (1993) A time integration algorithm for structural dynamics with improved numerical dissipation: the generalized-α method. J Appl Mech 60(2):371–375

Clauss G, Lehmann E, Östergaard C (1992) Offshore structures—volume I: conceptual design and hydromechanics. Springer, London. https://doi.org/10.1007/978-1-4471-3193-9

Clauss G, Lehmann E, Östergaard C (1994) Offshore structures—volume II: strength and safety for structural design. Springer, London. https://doi.org/10.1007/978-1-4471-1998-2

Cozzone AJ (2010) Proteins: fundamental chemical properties. Wiley, Hoboken. https://doi.org/10.1002/9780470015902.a0001330.pub2

Dalton G, Bardócz T, Blanch M, Campbell D, Johnson K, Lawrence G, Lilas T, Friis-Madsen E, Neumann F, Nikitas N, Ortega ST (2019) Feasibility of investment in blue growth multiple-use of space and multi-use platform projects; results of a novel assessment approach

and case studies. Renew Sustain Energy Rev 107:338–359. https://doi.org/10.1016/j.rser.2019.01.060

Dean RG, Dalrymple RA (1991) Advanced series on ocean engineering: volume 2 water wave mechanics for engineers and scientists. World Scientific, Singapore. https://doi.org/10.1142/1232

Delaux S, Stevens CL, Popinet S (2010) High-resolution computational fluid dynamics modelling of suspended shellfish structures. Environ Fluid Mech 11(4):405–425. https://doi.org/10.1007/s10652-010-9183-y

DIN-EN:12385–4:2008–06 (2008) Steel wire ropes—safety—part 4: stranded ropes for general lifting applications. Beuth Verlag, Berlin (German version EN)

Dinkler D (2020) Einführung in die Strukturdynamik. Springer Fachmedien Wiesbaden, Wiesbaden. https://doi.org/10.1007/978-3-658-31845-1

Det Norske Veritas (2010) Recommended practice DNV-RP-C205: environmental conditions and environmental loads. DNV, Norway

DNV (2021) Marine aquaculture forecast—ocean future to 2050. https://www.dnv.com/Publications/marine-aquaculture-forecast-to-2050-202391

Fredriksson DW, Swift M, Irish JD, Tsukrov I, Celikkol B (2003) Fish cage and mooring system dynamics using physical and numerical models with field measurements. Aquac Eng 27(2):117–146. https://doi.org/10.1016/S0144-8609(02)00043-2

Gagnon M (2019) Self-organization and mechanical properties of mussel culture suspensions: a critical review. Aquac Eng 87:102024. https://doi.org/10.1016/j.aquaeng.2019.102024

Gagnon M, Bergeron P (2017) Observations of the loading and motion of a submerged mussel longline at an open ocean site. Aquac Eng 78(Part B):114–129. https://doi.org/10.1016/j.aquaeng.2017.05.004

Gambhir M, Batchelor BD (1978) Finite element study of the free vibration of 3-d cable networks. Int J Solids Struct 15:127–136

Gansel LC, Plew DR, Endresen PC, Olsen AI, Misimi E, Guenther J, Jensen O (2015) Drag of clean and fouled net panels–measurements and parameterization of fouling. PLoS ONE 10(7):e0131051. https://doi.org/10.1371/journal.pone.0131051

Gieschen R, Schwartpaul C, Landmann J, Fröhling L, Hildebrandt A, Goseberg N (2020) Large-scale laboratory experiments on mussel dropper lines in ocean surface waves. J Mar Sci Eng 9(1):29. https://doi.org/10.3390/jmse9010029

Goseberg N, Chambers MD, Heasman K, Fredriksson D, Fredheim A, Schlurmann T (2017) Technological approaches to longline-and cage-based aquaculture in open ocean environments In: Buck BH, Langan R (eds) Aquaculture perspective of multi-use sites in the open ocean. Springer, Cham, pp 71–95

Gosling E (2008) *Bivalve molluscs*: biology, ecology and culture. Wiley, Hoboken

Gren IM, SällS Aklilu AZ, Tirkaso W (2018) Does mussel farming promote cost savings and equity in reaching nutrient targets for the Baltic sea? Water 10(11):1682

Heasman KG, Scott N, Smeaton M, Goseberg N, Hildebrandt A, Vitasovich P, Elliot A, Mandeno M, Buck BH (2021) New system design for the cultivation of extractive species at exposed sites—part 1: system design, deployment and first response to high-energy environments. Appl Ocean Res 110:102603. https://doi.org/10.1016/j.apor.2021.102603

Hickman R (1979) Allometry and growth of the green-lipped mussel *Perna canaliculus* in New Zealand. Mar Biol 51:311–327. https://doi.org/10.1007/BF00389210

Holthuijsen LH (2007) Waves in oceanic and coastal waters. Cambridge University Press, Cambridge. https://doi.org/10.1017/CBO9780511618536

Huu-Tai T, Seung-Eock K (2011) Nonlinear static and dynamic analysis of cable structures. Finite Elem Anal Des 47:237–246

Isbert W, Lindemann C, Lemburg J, Littmann M, Tegethoff K, Goseberg N, Durst S, Schürenkamp D, Buck BH (2023) A conceptual basis for surveying fouling communities at exposed and protected sites at sea: feasible designs with exchangeable test bodies for in-situ biofouling collection. Appl Ocean Res 136:103572

Knysh A, Tsukrov I, Chambers M, Swift MR, Sullivan C, Drach A (2020) Numerical modeling of submerged mussel longlines with protective sleeves. Aquac Eng 88:102027. https://doi.org/10.1016/j.aquaeng.2019.102027

Krause G, Brugere C, Diedrich A, Ebeling MW, Ferse SC, Mikkelsen E, Agúndez JA, Stead SM, Stybel N, Troell M (2015) A revolution without people? Closing the people-policy gap in aquaculture development. Aquaculture 447:44–55. https://doi.org/10.1016/j.aquaculture.2015.02.009

Landmann J, Ongsiek T, Goseberg N, Heasman K, Buck BH, Paffenholz JA, Hildebrandt A (2019) Physical modelling of blue mussel dropper lines for the development of surrogates and hydrodynamic coefficients. J Mar Sci Eng 7(3):65. https://doi.org/10.3390/jmse7030065

Landmann J, Fröhling L, Gieschen R, Buck BH, Heasman K, Scott N, Smeaton M, Goseberg N, Hildebrandt A (2021) Drag and inertia coefficients of live and surrogate shellfish dropper lines under steady and oscillatory flow. Ocean Eng 235:109377. https://doi.org/10.1016/j.oceaneng.2021.109377

Landmann J, Fröhling L, Gieschen R, Buck BH, Heasman K, Scott N, Smeaton M, Goseberg N, Hildebrandt A (2021) New system design for the cultivation of extractive species at exposed sites—part 2: experimental modelling in waves and currents. Appl Ocean Res 113:102749. https://doi.org/10.1016/j.apor.2021.102749

Mascorda Cabre L, Hosegood P, Attrill MJ, Bridger D, Sheehan EV (2021) Offshore longline mussel farms: a review of oceanographic and ecological interactions to inform future research needs, policy and management. Rev Aquac 13(4):1864–1887. https://doi.org/10.1111/raq.12549

Morison J, Johnson J, Schaaf S (1950) The force exerted by surface waves on piles. J Pet Technol 2(05):149–154. https://doi.org/10.2118/950149-g

Mèhautè B (1976) An introduction to hydrodynamics and water waves. Springer, Berlin. https://doi.org/10.1007/978-3-642-85567-2

Neumann B, Vafeidis AT, Zimmermann J, Nicholls RJ (2015) Future coastal population growth and exposure to sea-level rise and coastal flooding—a global assessment. PLoS ONE 10(3):e0118571. https://doi.org/10.1371/journal.pone.0118571

NOAA (2011) Marine aquaculture policy. https://media.fisheries.noaa.gov/2021-01/2011-noaa-marine-aquaculture-policy.pdf?VersionId=null

Nobakht-Kolur F, Zeinoddini M, Aliakbari T, Bahram M (2021) Wave attenuation/build-up around and inside marine fouled floating aquaculture cages under regular wave regimes. J Ocean Eng Mar Energy 7(1):59–81. https://doi.org/10.1007/s40722-021-00186-y

Nobakht-Kolur F, Zeinoddini M, Ghalebi A (2021) Hydrodynamic forces in marine-fouled floating aquaculture cages: physical modelling under irregular waves. J Fluids Struct 105:103331. https://doi.org/10.1016/j.jfluidstructs.2021.103331

Petersen JK, Hasler B, Timmermann K, Nielsen P, Torring DB, Larsen MM, Holmer M (2014) Mussels as a tool for mitigation of nutrients in the marine environment. Mar Pollut Bull 82(1):137–143. https://doi.org/10.1016/j.marpolbul.2014.03.006

Plew D, Stevens C, Spigel R, Hartstein ND (2005) Hydrodynamic implications of large offshore mussel farms. IEEE J Ocean Eng 30(1):95–108. https://doi.org/10.1109/joe.2004.841387

Plew DR, Enright MP, Nokes RI, Dumas JK (2009) Effect of mussel bio-pumping on the drag on and flow around a mussel crop rope. Aquac Eng 40(2):55–61. https://doi.org/10.1016/j.aquaeng.2008.12.003

Raed K, Guedes Soares C (2018) Variability effect of the drag and inertia coefficients on the Morison wave force acting on a fixed vertical cylinder in irregular waves. Ocean Eng 159:66–75. https://doi.org/10.1016/j.oceaneng.2018.03.066

Raman-Nair W, Colbourne B (2003) Dynamics of a mussel longline system. Aquac Eng 27(3):191–212. https://doi.org/10.1016/S0144-8609(02)00083-3

Raman-Nair W, Colbourne B, Gagnon M, Bergeron P (2008) Numerical model of a mussel longline system: coupled dynamics. Ocean Eng 35(13):1372–1380. https://doi.org/10.1016/j.oceaneng.2008.05.008

Schoefs F, Bakhtiari A, Ameryoun H (2022) Evaluation of hydrodynamic force coefficients in presence of biofouling on marine/offshore structures, a review and new approach. J Mar Sci Eng 10(5):558. https://doi.org/10.3390/jmse10050558

Stevens C, Plew D, Hartstein N, Fredriksson D (2008) The physics of open-water shellfish aquaculture. Aquac Eng 38(3):145–160. https://doi.org/10.1016/j.aquaeng.2008.01.006

Stokes GG (2009) On the theory of oscillatory waves, Cambridge library collection - mathematics, vol 1. Cambridge University Press, Cambridge, pp 197–229. https://doi.org/10.1017/CBO9780511702242.013

Theophahatos A (1988) Marine growth and the hydrodynamic loading of offshore structures. University of Strathclyde, Glasgow

Tsukrov II, Ozbay M, Swift MR, Celikkol B, Fredriksson DW, Baldwin K (2000) Open ocean aquaculture engineering: numerical modeling. Mar Technol Soc J 34(1):29–40. https://doi.org/10.4031/MTSJ.34.1.4

UN (2023) United nations, DESA, population division, world population prospects 2022. https://population.un.org/wpp/Graphs/DemographicProfiles/Line/900

Wang G, Martin T, Huang L, Bihs H (2022) An improved screen force model based on CFD simulations of the hydrodynamic loads on knotless net panels. Appl Ocean Res 118:102965

Wolfram J, Naghipour M (1999) On the estimation of Morison force coefficients and their predictive accuracy for very rough circular cylinders. Appl Ocean Res 21(6):311–328. https://doi.org/10.1016/S0141-1187(99)00018-8

Wolfram J, Theophanatos A (1990) Marine roughness and fluid loading. In: Environmental forces on offshore structures and their predictions: proceedings of an international conference, OnePetro, pp 145–160

Xu Z, Qin H, Li P, Liu R (2020) Computational fluid dynamics approaches to drag and wake of a long-line mussel dropper under tidal current. Sci Prog 103(1):003685041990123. https://doi.org/10.1177/0036850419901235

Zhao YP, Yang H, Bi CW, Chen QP, Dong GH, Cui Y (2019) Hydrodynamic responses of longline aquaculture facility with lantern nets in waves. Aquac Eng 86:101996. https://doi.org/10.1016/j.aquaeng.2019.101996

Zhu L, Huguenard K, Zou QP, Fredriksson DW, Xie D (2020) Aquaculture farms as nature-based coastal protection: random wave attenuation by suspended and submerged canopies. Coast Eng 160:103737. https://doi.org/10.1016/j.coastaleng.2020.103737